

Accepted by *The Astrophysical Journal Letters* 2001 Feb 24

Eccentric Nuclear Disks with Self Gravity: Predictions for the Double Nucleus of M31

Robert M. Salow and Thomas S. Statler

Department of Physics and Astronomy, 251B Clippinger Research Laboratories, Ohio University, Athens, OH 45701, USA

ABSTRACT

We present a method for constructing models of weakly self-gravitating, finite dispersion eccentric stellar disks around central black holes. The disk is stationary in a frame rotating at a constant precession speed. The stars populate quasiperiodic orbits whose parents are numerically integrated periodic orbits in the total potential. We approximate the quasiperiodic orbits by distributions of Kepler orbits dispersed in eccentricity and orientation, using an approximate phase space distribution function written in terms of the Kepler integrals of motion. We show an example of a model with properties similar to those of the double nucleus of M31. The properties of our models are primarily determined by the behavior of the periodic orbits. Self-gravity in the disk causes these orbits to assume a characteristic radial eccentricity profile, which gives rise to distinctive multi-peaked line-of-sight velocity distributions (LOSVDs) along lines of sight near the black hole. The multi-peaked features should be observable in M31 at the resolution of STIS. These features provide the best means of identifying an eccentric nuclear disk in M31, and can be used to constrain the disk properties and black hole mass.

Subject headings: galaxies: individual (M31)—galaxies: kinematics and dynamics—galaxies: nuclei

1. Introduction

Hubble Space Telescope (HST) images have resolved the nucleus of M31 into two distinct brightness peaks separated by $\sim 0''.49$ (Lauer et al. 1993, 1998). The optically fainter peak, P2, is located near a UV-bright cluster, which is thought to be the true location of the bulge photometric center and a supermassive black hole (BH; King et al. 1995; Kormendy & Bender 1999, hereafter KB99). The off-center peak, P1, appears to be an intrinsic component of the nucleus, rather than an intruding object (King et al. 1995, KB99). The currently favored model for the double nucleus (Tremaine 1995, hereafter T95) consists of an eccentric nuclear disk of stars on apse-aligned Kepler orbits (see Emsellem & Combes 1997 for an alternative). P1 represents the part of the disk near apocenter, where slower moving stars accumulate.

T95's disk is represented by three aligned Keplerian ringlets with outwardly decreasing eccentricities. New data from the Canada-France-Hawaii Telescope (CFHT) Subarcsecond Imaging Spectrograph (SIS) (KB99) are consistent with predicted asymmetries in the T95 model, including the offset rotation center, the asymmetric rotation amplitudes, the low dispersion at P1, and the dispersion peak near P2. The *HST* Faint Object Camera (FOC) observations of Statler et al. (1999, hereafter SKCJ) resolve the rotation curve and verify the existence of the dispersion peak, which has $\sim 400 \text{ km s}^{-1}$ amplitude at FOC resolution.

One-dimensional kinematic profiles from Space Telescope Imaging Spectrograph (STIS) spectra and two-dimensional data from the OASIS instrument on the CFHT (Bacon et al. 2001, hereafter B01) are both consistent with the FOC kinematics and the eccentric disk picture, when the data sets are spatially registered.

T95’s conceptual model needs to be extended to include self-gravity and finite velocity dispersion. Sridhar & Touma (1999, hereafter ST99) explore orbits in Kepler potentials with lopsided perturbations and find a class of periodic loop orbits elongated in the same sense as the perturbation. They point out that the nearly elliptical periodic parents of such orbits can be seen as the backbone of an eccentric disk with self-gravity and finite dispersion. Statler (1999, hereafter S99) computes periodic loop orbits for a uniformly precessing Tremaine-like disk model. He predicts a characteristic non-monotonic radial eccentricity distribution for the periodic orbits, resulting in a disk structure significantly different from that of the original T95 model. B01 present numerical simulations of an $m = 1$ mode in a cold disk with a central BH. They find a similar eccentricity structure to that predicted by S99. Tremaine (2001) studies slow $m = 1$ modes in axisymmetric nearly Keplerian disks using linear perturbation theory. He finds stable modes which have a different eccentricity structure from that seen by either S99 or B01.

In this *Letter*, we construct approximate self-consistent eccentric disk models with self-gravity and finite velocity dispersion. The details of model construction are described in § 2. We then briefly discuss the properties of such models in § 3. We show in § 4 that the line of sight velocity distributions (LOSVDs) on particular lines of sight have unusual bimodal shapes, and can be used to identify the presence of an eccentric disk in M31. Finally, § 5 discusses the connection with other work.

2. Model Construction

We postulate a disk whose density distribution is fixed in a frame rotating at constant angular speed Ω about a BH of mass M_\bullet . The disk is built from quasiperiodic loops (ST99) that librate about periodic parents. The latter are nearly Kepler ellipses in the rotating frame for small disk masses. We approximate the quasiperiodic orbits about a sequence of parents by a distribution of Kepler orbits dispersed in eccentricity and orientation, using the distribution function (DF)

$$f(a, e, \gamma) = F(a) \exp \left\{ -\frac{[e - e_0(a)]^2}{2\sigma_e^2} \right\} \exp \left[-\frac{\gamma^2}{2\sigma_\gamma^2} \right]. \quad (1)$$

In equation (1) the semimajor axis a , the eccentricity e , and γ , the angle between the disk major axis and the Runge-Lenz vector $\vec{A} = \vec{v} \times \vec{h} - GM\hat{r}$, are integrals of motion in the unperturbed potential. The function $e_0(a)$ describes the sequence of parent orbits that form the backbone of the disk. The constants σ_e and σ_γ are the dispersions in e and γ . The function $F(a)$, giving the mass per unit interval of semimajor axis, controls the radial mass distribution. We adopt

$$F(a) = \max(a - 1, 0) \exp \left[-\frac{(a - a_0)^2}{2\sigma_a^2} \right], \quad (2)$$

where the constant a_0 sets the length scale for the model, and σ_a is the width of the density distribution. This $F(a)$ is chosen to produce density figures with limited radial extent and strong central density minima. It is not intended to fit in detail the surface photometry of the M31 nucleus, where the putative disk is not radially truncated. Nonetheless, the models do reproduce many of the observed characteristics of the inner regions, the predicted LOSVDs at small radii being essentially independent of the outer disk structure.

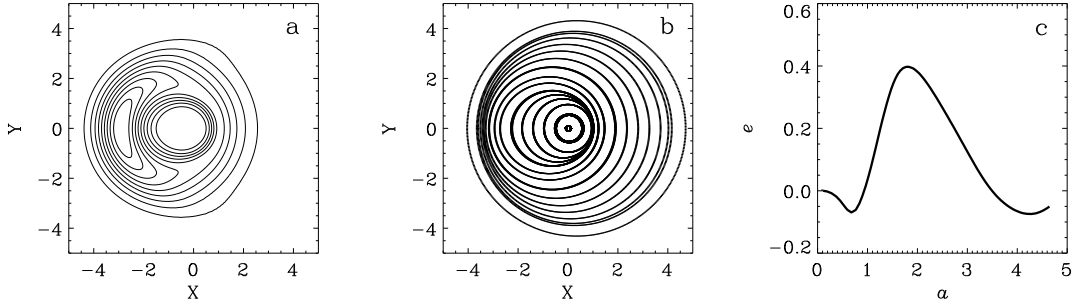


Fig. 1.— (a) Density contours for the fiducial model. Contours are at 0.1, 0.2, ..., 1.0 of the maximum density. The central point mass is at (0,0), near the point of minimum density. (b) Uniformly precessing periodic orbits in the total potential. The radial variation of eccentricity is a consequence of disk self-gravity. (c) Eccentricity of the orbits in (b) plotted against semi-major axis; this is the function $e_0(a)$ in equation (1).

Starting from an initial guess for $e_0(a)$, the DF is written in terms of position and velocity using the Keplerian relations for a , e , and γ , and integrated over velocity to obtain the density, normalized for a total disk mass m . The potential is found using a standard Fourier method on a cartesian grid. The disk potential is added to that of the central BH, and the combined potential is rotated at frequency Ω about the center of mass. We then numerically integrate to find a new set of periodic parent orbits, which become the backbone for the next iteration. Iterations are terminated when the fractional change in the density per iteration is $< 5\%$ everywhere and $< 1\%$ on average. The results are not sensitive to the initial $e_0(a)$.

3. Model Properties

A model is specified by the parameters $\epsilon = m/M_\bullet$, Ω , σ_a , σ_e , and σ_γ . Models are computed in dimensionless units where $G = M_\bullet = 1$ and $a_0 = 2$. Figures 1, 2, and 3 show results for a fiducial model with $\epsilon = 0.03$, $\Omega = 0.015$, $\sigma_a = 1.0$, $\sigma_e = 0.175$, and $\sigma_\gamma = 0.4$.

Figure 1a shows a contour plot of the surface density. The disk is non-axisymmetric, with a density maximum near $x = -3$. The outer cutoff reflects the adopted form of $F(a)$. Figure 1b shows the set of periodic parent orbits. These orbits have the non-monotonic run of eccentricity with semimajor axis argued for by S99 (his Fig. 3). The sequence is described by the function $e_0(a)$, plotted in Figure 1c. Notice that $e_0(a)$ peaks near $a = a_0$, and becomes negative at larger a ; orbits with negative eccentricities have apocenters at $x > 0$. The basic shape of this function is characteristic of all the models we have computed.

Observable velocity moments can be obtained by integrating the DF in equation (1). Projected profiles on the disk major axis are shown in Figure 2. For the sake of realism we have scaled the model to the parameters of M31, and simulated the FOC observations. The bulge and central cusp are approximated by a single spherical, non-rotating η -model (Tremaine et al. 1994) that includes the influence of the BH.¹ The

¹The effect of the bulge potential on the disk is ignored; the bulge-induced precession frequencies of Kepler orbits in the absence of the disk potential are < 0.001 .

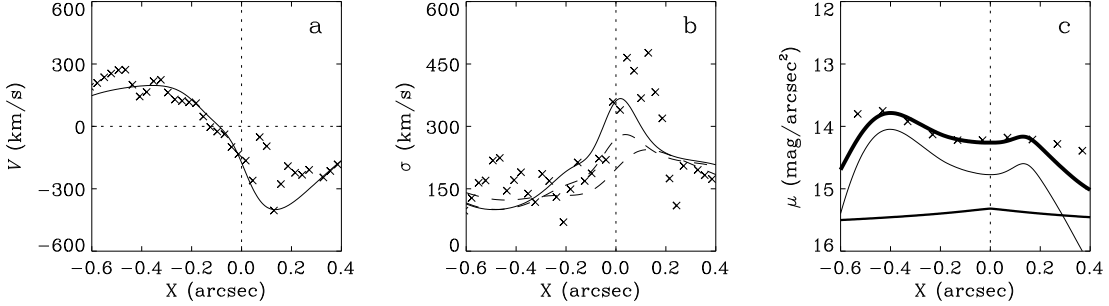


Fig. 2.— Major axis kinematic and photometric profiles for the fiducial model, scaled to M31. The added bulge model has $\eta = 2.28$ and scale length $r_0 = 85''$, scaled to resemble B01’s MGE model from $4''$ to $10''$. Disk and bulge have V -band $M/L = 4$ (solar units, T95), and $M_\bullet = 3.2 \times 10^7 M_\odot$. The length scale is set by the $0''.44$ separation between P1 and the UV peak (B01). (a) Rotation curve and (b) Velocity dispersion convolved to the resolution of FOC (solid line). Crosses show FOC profiles; error bars are omitted for clarity. Dashed lines in (b) show profiles for $0''.1$ and $0''.35$ slit widths. (c) Surface brightness profiles for the disk (thin line), bulge (medium line), and the total (heavy line) integrated over a $0''.35$ wide slice, with HST I -band data (crosses; from Fig. 8 of KB99, $14.4 \text{ mag arcsec}^{-2}$ zero point, includes $12.56, 1.37$, and $0.47 \text{ mag arcsec}^{-2}$ shifts for the I -band zero point (J. Kormendy, private communication), $V-I$, and compensation for the model’s truncation within the $0''.35$ slice, respectively.

disk is inclined at 77° , and the line of sight is perpendicular to the major axis. Moderate rotations of the model in the disk plane affect the results only slightly. The observables are integrated over the FOC slit as projected onto the disk plane.

The rotation curve and dispersion profile are shown as the solid lines in Figures 2a and 2b. Crosses show the FOC data for comparison; both profiles have been shifted by $+0''.025$ spatially and the rotation curve has been shifted upward by 30 km s^{-1} , as recommended by B01. Figure 2c shows the surface brightness profiles for the disk, bulge, and the sum, compared with I -band HST WFPC2 photometry. This model is able to reproduce many of the salient features in the observed profiles, even though it is not a rigorous fit.² These features include the relative brightnesses of P1 and P2, the shape of the rotation curve, the offset of the rotation center, and the low dispersion of P1. A dispersion spike appears near P2 in both model and data. Its detailed properties are problematic, and will be discussed in § 5.

Changing the parameters from their fiducial values alters the disk properties. Axisymmetry decreases monotonically with increasing ϵ/Ω . From the ratio of the projected surface brightness peaks, we find that disks become axisymmetric to within 5% for $\epsilon/\Omega < 0.6$. M31-like models require $\epsilon/\Omega > 1$. We find converged models only for $0.5 \lesssim \epsilon/\Omega \lesssim 2.0$ and $\epsilon \lesssim 0.21$.

Disks are also made more axisymmetric by increasing σ_γ , which spreads the orientations of the dispersed ellipses. Increasing σ_e , on the other hand, makes the disk more lopsided, essentially because the contrast in linear density on a single Kepler orbit, $\rho_{apo}/\rho_{peri} = (1+e)/(1-e)$, is a concave-up function of e . We find empirically that we need $\sigma_e \geq 0.15$ and $\sigma_\gamma \leq 0.6$ to produce M31-like models with large eccentric density peaks. Finally, the effect of increasing σ_a is to broaden the mass distribution radially, while having minimal effect on the kinematics or axisymmetry.

²Because the disk models are radially truncated, the fit to the data for $x < -0''.6$ and $x > 0''.2$ is poor.

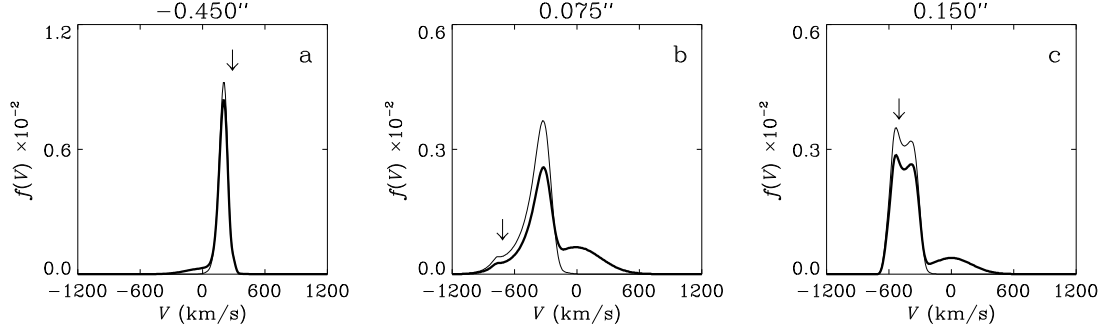


Fig. 3.— LOSVDs for the M31-scaled fiducial model, integrated over a $0''.1$ wide slit and convolved to STIS resolution. The thin (thick) line shows the LOSVD without (with) the bulge contribution. Arrows mark the circular speed at the tangent point. (a) LOSVD through P1, $x = -0''.450$ from the UV peak, similar to that expected for a cold, axisymmetric disk with outwardly decreasing density. (b) LOSVD through P2, $x = 0''.075$ from the UV peak. The peak at supra-circular velocity results from the eccentricity structure, the large peak from the outwardly increasing density. (c) LOSVD $0''.075$ past P2, $x = 0''.150$ from the UV peak. The density decreases outward; the smaller peak is from the eccentricity gradient.

4. LOSVDs

All of our models share the same characteristic eccentricity structure for the parent periodic orbits (Fig. 1b,c). The eccentricity structure, modulated by the velocity dispersion, determines the LOSVDs. We find that the LOSVDs along certain lines of sight hold the key for identifying disks of this type and for measuring their basic parameters.

In Figure 3 we show three LOSVDs for the fiducial model, oriented as in Figure 2 and scaled to the parameters of M31. The thick and thin lines show the LOSVDs with and without the bulge model described in § 3. We approximate the bulge LOSVD by a Gaussian with the correct projected dispersion of the adopted η -model, ignoring the higher moments. The LOSVDs are convolved to approximately the spatial and spectral resolution of the STIS data, assuming Gaussian point- and line-spread functions.

Figure 3a shows the LOSVD for a line of sight through P1. The shape is similar to that expected for a cold, axisymmetric disk. The LOSVD peaks near the tangent point velocity, and shows an extended tail arising from material in front or behind the tangent point. The tail in ordinary disks is weak when the density decreases outward. The model LOSVD has this form; the bulge contribution is minimal, due to the large disk density at P1.

Figure 3b shows the LOSVD for a line of sight through P2, $0''.075$ on the opposite side of the central mass. Here the disk LOSVD is double peaked. The peak at large negative velocities corresponds to the tangent point, which falls near the pericenters of orbits with substantial eccentricities (Fig. 1b), creating a peak at supra-circular velocities. The peak at smaller negative velocities has the same origin as the low velocity tail in P1, but the slope is reversed for two reasons: first, the line of sight traverses the disk's central hole, where the density increases outward; second, the outward decrease in eccentricity amplifies the line of sight velocity of material in front or behind the tangent point. The former effect dominates along this line of sight, so the location of the low speed cutoff is a function of the slit width.

Figure 3c shows the LOSVD for a line of sight an additional $0''.075$ past P2. The LOSVD changes

significantly over very small spatial scales, owing both to the near Keplerian potential and the negative gradient in $e_0(a)$. The tangent point peak has shifted by $\sim 250 \text{ km s}^{-1}$ over $0''.075$. Roughly $3/4$ of this shift results from the Keplerian drop in circular speed, and the remaining $1/4$ from the eccentricity gradient. The peak at slower speeds results entirely from the eccentricity gradient, since the line of sight does not traverse the central hole.

All of our disk models show bimodal LOSVDs in projection near the secondary density peak. *These LOSVDs are generic to the models, arising from the density and eccentricity structure, and should be observable at STIS resolution.* They therefore provide the best means of unambiguously identifying an eccentric nuclear disk in M31.

5. Discussion

We have presented a method for constructing approximate models of near-Keplerian eccentric disks with self gravity and finite velocity dispersion, appropriate to the M31 double nucleus.³ The properties of the models are dictated by the “backbone” periodic orbits, which show a characteristic radial profile (S99), giving rise to distinctive LOSVDs for lines of sight through the secondary density maximum, near the central mass.

The details of the dispersion peak (Figure 2b) deserve special mention. Its amplitude can be tuned by changing M_\bullet or other model parameters. The observed maximum, however, is offset from the UV cluster by a distance that depends on resolution, increasing from $0''.1$ for the FOC data to $0''.2$ for the OASIS data (B01). We find that, while the model peak also shifts away from the origin with widening slit width (Fig. 2b, dashed lines), the offset is smaller by $\sim 0''.06$. It is difficult to move the dispersion maximum away from the position of the BH. The bulge dispersion must peak at the origin if the BH dominates the gravity. Either this peak will shine through the density minimum in the disk, or disk material orbiting at very small radii will produce the same effect. We see two possible sources for the discrepancy in position: first, that the models are incomplete, missing some essential bit of physics; second, that the blue cluster is a red herring, not marking the true location of the BH.

Our fiducial model is similar to B01’s N -body simulation of a strong $m = 1$ mode in a cold, thin disk with a central BH. The peak locus in their particle density plot in the (e, a) plane is similar to our function $e_0(a)$ (Fig. 1c). B01 note in particular that the pericenters of orbits in the inner and outer parts of the disk are in phase opposition, as predicted by S99. They find a pattern speed of $\Omega = 3 \text{ km s}^{-1} \text{ pc}^{-1}$, compared to our fiducial model with $\Omega_p = 13.6 \text{ km s}^{-1} \text{ pc}^{-1}$. On the other hand, Sambhus and Sridhar (2000), using a variant on the Tremaine & Weinberg (1984) method, obtain $20 \pm 12 \text{ km s}^{-1} \text{ pc}^{-1}$ and $34 \pm 8 \text{ km s}^{-1} \text{ pc}^{-1}$ from two different fits to the bulge. Thus neither data nor models at present provide good constraints on the pattern speed.

How such a large $m = 1$ mode could arise remains problematic. B01 indicate that the nonlinear modes seen in their simulations can grow spontaneously from axisymmetric initial conditions. On the other hand, Tremaine (2001) examines slowly precessing $m = 1$ modes in nearly Keplerian disks, concluding that all such disturbances are stable and tend not to have the eccentricity structure shared by our models and B01’s

³The model does not show a “P1 wiggle” in the rotation curve, which S99 cites as a possible signature of self-gravity. Contrary to S99’s speculation, this feature is washed out in all but the coldest models. Since the P1 wiggle is not seen in the STIS rotation curve either, we conclude that it is probably an artifact of the FOC data.

simulation.

The true test of the eccentric disk picture for the M31 nucleus lies in the line of sight velocity distributions near P2. Our models predict that the LOSVDs in this region should be distinctive and probably bi- or even tri-modal. The widths of the peaks, and how they shift in velocity and vary in amplitude as a function of position, will constrain the disk's velocity dispersion and its density and eccentricity structure. Extracting the full LOSVD from the M31 spectra demands much higher signal-to-noise (S/N) than obtaining V and σ alone. B01 defer discussion of the higher moments in the STIS data because of S/N issues, though preliminary results look intriguing (E. Emsellem, private communication).

This work was supported by NSF CAREER grant AST 97-03036. We thank Scott Tremaine for providing code to compute self-consistent η models, and John Kormendy, Ralf Bender, and the referee, Eric Emsellem, for helpful comments.

REFERENCES

Bacon, R., Emsellem, E., Combes, F., Copin, Y., Monnet, G., & Martin, P. 2001, A&A, submitted; astro-ph/0010567 (B01)

Emsellem, E. & Combes, F. 1997, A&A, 323, 674

King, I. R., Stanford, S. A., & Crane, P. 1995, AJ, 109, 164

Kormendy, J., & Bender, R. 1999, ApJ, 522, 772 (KB99)

Lauer, T. R., Faber, S. M., Groth, E. J., Shaya, E. J., Campbell, B., Code, A., Currie, D. G., Baum, W. A., Ewald, S. P., Hester, J. J., Holtzman, J. A., Kristian, J., Light, R. M., & Westphal, J. A. 1993, AJ, 106, 1436

Lauer, T. R., Faber, S. M., Ajhar, E. A., Grillmair, C. J., & Scowen, P. A. 1998, AJ, 116, 2263

Sambhus, N. & Sridhar, S. 2000, ApJ, 539, L17

Sridhar, S. & Touma, J. 1999, MNRAS, 303, 483 (ST99)

Statler, T. S. 1999, ApJ, 524, L87 (S99)

Statler, T. S., King, I. R., Crane, P., & Jedrzejewski, R. I. 1999, AJ, 117, 894 (SKCJ)

Tremaine, S., Richstone, D. O., Byun, Y.-I., Dressler, A., Faber, S. M., Grillmair, C., Kormendy, J., & Lauer, T. R. 1994, AJ, 107, 634

Tremaine, S. 1995, AJ, 110, 628 (T95)

Tremaine, S. 2001, AJ, in press (astro-ph/0011571)

Tremaine, S. & Weinberg, M. D. 1984, ApJ, 282, L5